



Review article

FLIM reveals alternative EV-mediated cellular up-take pathways of paclitaxel

H. Saari^{a,1}, E. Lisitsyna^{a,b,1}, K. Rautaniemi^b, T. Rojalin^{a,2}, L. Niemi^{a,3}, O. Nivaro^a, T. Laaksonen^{a,b}, M. Yliperttula^{a,c,*}, E. Vuorimaa-Laukkanen^b

^a Faculty of Pharmacy, Division of Pharmaceutical Biosciences, University of Helsinki, 00014 Helsinki, Finland

^b Laboratory of Chemistry and Bioengineering, Tampere University of Technology, 33720 Tampere, Finland

^c Pharmaceutical Technology and Biopharmaceutics Department of Pharmaceutical and Pharmacological Sciences of University of Padova, via F. Marzolo 5, 35131 Padova, Italy

ARTICLE INFO

Keywords:

Extracellular vesicles
Microvesicles
Exosomes
Paclitaxel
Drug delivery
Prostate
Cancer
Fluorescence lifetime imaging microscopy

ABSTRACT

In response to physiological and artificial stimuli, cells generate nano-scale extracellular vesicles (EVs) by encapsulating biomolecules in plasma membrane-derived phospholipid envelopes. These vesicles are released to bodily fluids, hence acting as powerful endogenous mediators in intercellular signaling. EVs provide a compelling alternative for biomarker discovery and targeted drug delivery, but their kinetics and dynamics while interacting with living cells are poorly understood. Here we introduce a novel method, fluorescence lifetime imaging microscopy (FLIM) to investigate these interaction attributes. By FLIM, we show distinct cellular uptake mechanisms of different EV subtypes, exosomes and microvesicles, loaded with anti-cancer agent, paclitaxel. We demonstrate differences in intracellular behavior and drug release profiles of paclitaxel-containing EVs. Exosomes seem to deliver the drug mostly by endocytosis while microvesicles enter the cells by both endocytosis and fusion with cell membrane. This research offers a new real-time method to investigate EV kinetics with living cells, and it is a potential advancement to complement the existing techniques. The findings of this study improve the current knowledge in exploiting EVs as next-generation targeted drug delivery systems.

1. Introduction

Extracellular vesicles (EV) are a heterogeneous group of phospholipid bilayer-bound vesicles secreted by prokaryotic and eukaryotic cells [1, 2]. EVs can be classified with respect to their biogenesis pathways and various biochemical and –physical attributes into three major groups, although several other types of EVs exist as well [3–5]. Exosomes (EXOs) are a sub-group of EVs generated by reverse budding from the peripheral membrane of multivesicular bodies (MVB) within endosomal network and released when MVBs fuse with the plasma membrane. The size of EXOs in MVBs before secretion varies in the range 40–120 nm. Microvesicles (MV) are derivatives of plasma membrane budding with wider size distribution of approximately 50–1000 nm. Lastly, apoptotic vesicles (APO) are EVs of up to 2000 nm in diameter and originating from plasma membrane shedding of apoptotic cells [6]. We delimit the debate herein to EXOs and MVs as they are the two prominent EV sub-populations under immense

investigation throughout the field, and our present work focuses on characterizing the sub-cellular mobility of these EV types.

Virtually all cells secrete EVs at normal physiological conditions as well as during pathological states. EVs are pertinent mediators e.g. in immune system responses [7, 8], cancer progression and metastasis [9–13], infections [14–16] and inflammatory diseases [17]. EVs do not arbitrarily distribute in bodily fluids but they deliver nucleic acids, proteins, lipids and various small molecules via intercellular pathways to specific cellular targets. Due to their biological origin, EVs possess a unique natural content that allows for overcoming the known limitations of artificial liposomal drug carriers, such as potential liver toxicity or immunogenicity as well as targeting issues [18, 19]. Once delivered, the EV cargo can modulate various biological functions in target cells according to the payload instructions. These features make EVs a promising alternative to conventional liposome-based targeted drug delivery. They can be loaded with small or macromolecular drugs to accomplish specific therapeutic effects [20–22]. When used as drug

* Corresponding author at: Faculty of Pharmacy, Division of Pharmaceutical Biosciences, University of Helsinki, 00014 Helsinki, Finland.

E-mail address: Marjo.yliperttula@helsinki.fi (M. Yliperttula).

¹ Equal contribution

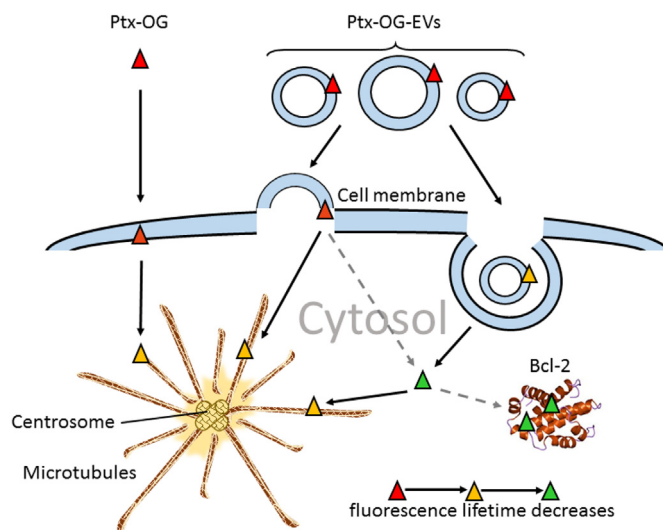
² Current affiliation: Department of Biochemistry and Molecular Medicine, University of California Davis, Sacramento, California 95,817, United States

³ Current affiliation: Orion Pharma, Espoo, Finland

delivery carriers, EVs' natural biogenesis and delivery mechanisms could be exploited in combination with surface chemistry modification to achieve desired pharmacokinetic distribution, metabolization and elimination profiles. However, the current mechanistic understanding of EV-mediated drug delivery is somewhat limited and there is an unmet need to develop novel methodologies to overcome these limitations. Most existing EV characterization techniques are best suited for investigating their biochemical contents [23–32], not for providing information on the EVs' kinetic and dynamic properties. Only confocal microscopy has been utilized to track the cellular uptake of EVs on a sub-cellular level [33], while flow cytometry (FC) has been employed to estimate the bulk uptake kinetics of EVs [34, 35], however FC cannot be used to distinguish between intracellular and surface-bound EVs. Thus, an intriguing question still remains unanswered: how to obtain sub-cellular insights in real time into the EV kinetics in the case of cellular uptake?

Fluorescence lifetime imaging microscopy (FLIM) is a technique to map the spatial distribution of excited state lifetimes in microscopic samples. Being minimally invasive, the method is widely used nowadays for biomedical applications, particularly for gaining information on molecular dynamics and interactions in single living cells [36–38]. Conventional fluorescence confocal (one or two-photon excitation) techniques use steady-state fluorescence intensity measurements to produce corresponding two or three-dimensional images. However, fluorescence intensity is strongly affected by a variety of environmental influences, such as strong background fluorescence of the living systems, quenching by other molecules, aggregation, energy transfer, and refractive index effects. This makes it difficult to interpret and quantify the intensity-based data, especially in complex samples such as cells or tissues. In FLIM the fluorescence lifetime (τ) of a probe molecule is measured as the rate of emission decay [39, 40] and the differences in the probe fluorescence decay times provide the contrast mechanism for FLIM images [41, 42]. The advantage of using FLIM in complex systems is that the calculated fluorescence lifetimes can provide significantly more information than the intensities. Since the excited state lifetime depends on the local physicochemical environment of the fluorophore, it is used for sensing inter- and intramolecular processes in living cells, such as protein and DNA binding events [43, 44], changes in pH [45], local viscosities [46], and the presence of such lifetime quenchers as ions or oxygen [47, 48]. FLIM delivers information about the environmental change around the fluorescent probe even when it mainly remains in the same spatial location (e.g. inside the cell) and its fluorescence intensity holds constant. Notably, the emission is an inherent property of the fluorophore, and therefore the fluorescence lifetime is not affected by the change in probe concentration, photobleaching, or light scattering. Additionally, the excited state lifetime is not influenced by internal settings of the instrument such as laser intensity or detector gain. Autofluorescence of biological structures such as mitochondria and lysosomes can be almost avoided by time-correlated single photon counting, i.e. TCSPC-based FLIM systems, utilized in the current study.

Only a few successful applications of excited state lifetime microscopy to monitor cellular uptake and release of a drug from the polyplexes [49, 50], and theranostics [51], have been recently reported. As yet, FLIM has not been utilized to investigate neither the EV cell-uptake processes as a function of time nor to investigate the intracellular trafficking of EVs. In this study, an anti-cancer drug, paclitaxel (Ptx), covalently labeled with Oregon Green (OG) fluorophore and loaded into EXOs or MVs is used to probe for various cellular uptake stages and intracellular trafficking of Ptx-OG and EV-Ptx-OG. Ptx-OG has been previously used in studying the intracellular kinetics of drugs, and Ptx-OG interaction with the microtubule network [52]. EV-mediated delivery of Ptx-OG has also been demonstrated earlier [35, 53–55] but the underlying sub-cellular mechanisms have not been meticulously explored. According to previous reports, EV uptake by recipient cells potentially occurs via endocytic pathway, phagocytosis,



Scheme 1. Experimental design and concept. Vesicles of different sizes illustrate the size heterogeneity of EV populations used in this study (SI Fig. S3A). Colors of Ptx-OG in the scheme (red, yellow and green) correspond to the color scale of FLIM images 2.0 ns to 4.5 ns. Solid arrows represent confirmed trafficking paths of the Ptx-OG-EVs and Ptx-OG inside the cell, dashed arrows are assumed pathways that require additional studies to prove.

micropinocytosis [33, 56], or, through a fusion process with the plasma membrane [57].

Paclitaxel belongs to the group of taxanes known to target microtubules, interacting with β -tubulin and consequently distracting microtubule dynamics by preventing their disassembly [58, 59]. On account of this, the microtubule network is expected to be labeled by Ptx-OG regardless the type of carrier (EXOs or MVs). As the EVs are processed in the endosomal network, their cargo has many alternative fates, including lysosomal degradation, recycling to the plasma membrane, exocytosis via the exosomes of the multivesicular bodies and additional intracellular trafficking at the trans-Golgi network, from which Ptx-OG could end up virtually anywhere in the cell, including the Bcl-2 expressing organs [60]. However, as EVs have also been shown to be able to fuse with the plasma membrane of the cell [61], in this case the delivery of Ptx-OG should appear similar to the delivery pattern of free Ptx-OG, since both would enter the cell through diffusion from the plasma membrane.

The concept of the study is illustrated in Scheme 1. Using FLIM for live-cell imaging, we demonstrate that the Ptx-OG trafficking in prostate cancer (PC) cells indeed utilize different intracellular pathways depending on the delivery system it is loaded into. Furthermore, we show that the intracellular release of Ptx-OG from the EV-carriers can be observed by monitoring OG fluorescence lifetime. We envisage that this FLIM-based platform may provide a powerful tool to study both the intracellular trafficking of EVs and Ptx-OG. In addition, the obtained results can open new perspectives for experts working with targeted drug delivery development and controlled drug release.

2. Materials and methods

2.1. Cell culturing

Gibco™ (ThermoFisher Scientific, Massachusetts, USA) reagents were used for cell culturing. For live-cell imaging human prostate cancer cell line PC-3 cells (ATCC, Virginia, USA) were cultured in T-75 flasks, using 10 ml of Ham's F-12 K (Kaighn's) Medium with 10% (v/v) FBS and 100 units/ml penicillin/ streptomycin. For PC-3 EV production CELLLine 1000 CE bioreactor flasks (Wheaton, New Jersey, USA) were used. The bioreactor upper compartment was filled with 750 ml of

Ham's F-12 K (Kaighn's) Medium with 10% (v/v) FBS, supplemented to a final concentration of 4.5 g/l glucose solution, and 100 units/ml penicillin/streptomycin. 15 ml of corresponding Ham's culture medium without FBS was used in the bioreactor's cell compartment to avoid FBS derived EVs. The culture medium containing EVs was collected once a week from the bioreactor's cell compartment, the cell compartment was washed three times with 15 ml of fresh medium to detach the excessive amount of cells, and 750 ml of fresh culture medium was changed to the upper compartment. The cells were cultured at +37 °C, 5% CO₂, 95% relative humidity.

2.2. EV isolation

EV isolation was performed using, differential ultracentrifugation. In brief, the medium was collected from the bioreactor's cell compartment, and consequently buoyant cells, cell fragments and big apoptotic vesicles were removed by centrifuging with Centrifuge 5810 R desktop centrifuge (Eppendorf, Hamburg, Germany) at 2500g for 25 min, +4 °C. Next, MVs were extracted from the supernatant by centrifuging with Beckman Coulter Optima LE-80 K ultracentrifuge, Type 50.2 Ti rotor (Coulter, California, USA) at 20000g for 1 h, +4 °C. EXOs were isolated from the supernatant by centrifuging with the same ultracentrifuge setting at 110000g for 2 h, +4 °C. Lastly, the supernatant was removed also from the EXO pellet. Both, the MV and EXO pellets were allowed to detach from the centrifuge tubes in 100 µl of DPBS buffer (ThermoFisher Scientific, Massachusetts, USA) overnight at +4 °C, followed by further purification in an iodixanol (Optiprep™, Sigma Aldrich) density gradient. In the current study we discriminate the EV populations according to the centrifugal force used for the isolation of each fraction and call them herein 20 K MVs and 110 K EXOs.

2.3. Iodixanol density gradient centrifugation

Iodixanol was buffered with DPBS and used to prepare a stepwise density gradient. In order to determine the buoyant density of EVs, the EV pellets produced in Section 2.2 were mixed with iodixanol into a final concentration of 40% with final volume of 2 ml and loaded at the bottom of a discontinuous iodixanol gradient prepared by overlaying 30%, 20% and 10% iodixanol 2 ml each and filling the rest of the centrifuge tube with buffer. The samples were then ultracentrifuged for 18.5 h with 200,000 g at +4 °C. 1 ml fractions were then collected from the top, discarding the bottom 2 ml. The EV-containing fractions were identified with NTA analysis, pooled and iodixanol was removed by diluting in 15 ml total volume of cold DPBS followed by serial ultrafiltration with Amicon Ultra-15 ultrafiltration units at +4 °C.

A simplified approach with iodixanol gradient was used for sample preparation in FLIM experiments. Here, EV-pellets were loaded on top of a gradient prepared by overlaying 700 µl of 10% iodixanol on top of 300 µl of 30% iodixanol in 1.5 ml ultracentrifuge tubes. The samples were then ultracentrifuged in rotor TLA-55 with Optima MAX-XP ultracentrifuge for three hours with 170,000 g at +4 °C. The resulting visible EV-band in the 10% and 30% interphase was then collected and iodixanol was removed by ultrafiltration as described above.

2.4. Nanoparticle tracking analysis (NTA)

The particle concentrations and size distributions of 20 K MVs and 110 K EXOs were analyzed using Nanosight LM-14 instrument (LCM14C, 405 nm laser, 60 mW, Nanosight, Salisbury, Great Britain) equipped with sCMOS camera (Hamamatsu Photonics K.K., Hamamatsu, Japan). The camera level was adjusted to 14, measurement time for one acquisition was 90 s and every sample was analyzed in triplicates. The results were analyzed using NanoSight NTA software (NanoSight Ltd., v. 3.0) with detection threshold set to 5.

2.5. Cell lysate preparation

Cell lysate of PC-3 cells was prepared from a T75 cell culture flask of PC-3 cells that were washed with ice-cold DPBS, followed by scraping them in ice-cold RIPA lysis buffer (ThermoFisher Scientific) supplemented with protease inhibitor cocktail (Sigma Aldrich). The samples were then incubated for 30 min at +4 °C under agitation followed by centrifugation with 16,000 g at +4 °C for 20 min, collecting the resulting supernatant.

2.6. Western blotting

The protein amount of EV samples prepared with iodixanol density gradient and PC-3 cell lysate were standardized using Pierce™ BCA protein assay kit (ThermoFisher Scientific) for the western blotting. A total of 20 µg of protein was prepared by heating in Laemmli denaturing sample buffer and ran with 4–20% Mini-PROTEAN® TGX™ Precast Protein Gel (BioRad, Hercules, CA, USA). The proteins were then transferred to a nitrocellulose membrane that was then blocked by incubating it in 5% bovine serum albumin (BSA, Sigma Aldrich) in 0.1% (v/v) TBS-Tween 20 (TBS-T) for one hour at room temperature under agitation. The membrane was then cut into strips according to the molecular weights of the proteins to be identified and the strips were incubated in their respective primary antibody solutions overnight at +4 °C under agitation. The primary antibody solutions (mouse anti-TSG101, BD Biosciences, Franklin Lakes, NJ, USA and mouse anti-Hsp70, BD Biosciences) were prepared in 5% BSA TBS-T by diluting them 1:500. After the incubation the membranes were washed three times in TBS-T, followed by incubation with HRP-conjugated secondary anti-mouse antibody (ECL™ Anti-mouse IgG, GE healthcare, Little Chalfont, UK) in TBS-T for one hour at RT. The membranes were then washed again three times in TBS-T and once in TBS, followed by a 5 min incubation in ECL substrate solution (Clarity™ Western ECL Substrate, BioRad) and imaged with BioSpectrum® imaging system (Ultra-Violet Products, Cambridge, UK).

2.7. EV labeling and loading

The molecular structure of Ptx-OG (Tubulin Tracker Green™, ThermoFisher Scientific, Massachusetts, USA) is presented in the Supplementary Information (SI) Fig. S1. The 20 K MVs and 110 K EXOs were labeled and loaded for FLIM imaging by adding 7.5 µl of 1 mM Ptx-OG to one milliliter of 20 K MV/110 K EXO suspension (20 K MV/110 K EXO particle concentration adjusted with DPBS to 1.5×10^{10} particles/ml), and by incubating the suspension protected from light for 60 min upon shaking at ambient temperature. Following the incubation, the excess of Ptx-OG was removed by centrifuging once with Optima MAX ultracentrifuge (MLA-130 rotor) at 110000 g for 180 min, +22 °C. The 20 K MV/110 K EXO pellets were resuspended in 50 µl of DPBS before the application to the cells. Loading of the EVs with Ptx-OG was estimated by ultra-performance liquid chromatography (UPLC, Acquity UPLC system, Waters, Massachusetts, USA), UPLC column CORTECS™ C18+ 2.1 × 50 mm with pore size 2.7 µm (Waters, Ireland). Flow rate was 0.5 ml/min. The sample injection volume was 5 µl. Gradient solution was phosphate buffer:acetonitrile with 40–80% of acetonitrile. Signal was detected at 290 nm with retention time 2.6 s. Ptx-OG loaded EVs were pretreated with 1% Triton X-100 and centrifuged at 1000 g for 5 min. Due to some losses of Ptx-OG loaded EVs after purification and intentional providing of small labeling densities to avoid fluorescence self-quenching events the small concentrations of Ptx-OG in EVs had fallen under the calibration curve according to UPLC data. This made it impossible to calculate the exact reliable values of the loading efficiencies. However, estimated loading of the EVs was over 50% in both 110 K EXOs and 20 K MVs.

After the Ptx-OG labeling and loading, the MV membranes were labeled with lipophilic DiD label (Biotium Inc., USA) for confocal

imaging. 1 μ l of DiD label was added to 1 ml of MV suspension (10^{10} particles/ml) and incubated for 30 min at +22 °C protected from light. Unbound DiD label was removed by centrifugation as described above.

2.8. Cell sample preparation for FLIM

One day before the imaging procedure 75,000 PC-3 cells were inoculated to a glass bottom 35 mm Petri dish, No. 0 coverslip, 10 mm glass diameter, coated with poly-D-lysine (MatTek, Massachusetts, USA). Medium was changed 2 h before the imaging. Free Ptx-OG as well as Ptx-OG loaded EVs were added into the medium of PC-3 cell culture at the microscope stage directly before imaging of the first time points (several minutes after the addition) followed by the further imaging for 24 h (Ptx-OG EVs) and 12 h (free Ptx-OG). A single cell was imaged every 2 h until the end of the experiment or until the cell detached. As the aim of the study was to monitor the trafficking of Ptx-OG and Ptx-OG-labeled EVs in the cells, the excess of the label was not washed out prior the FLIM measurements in contrast to the conventional sample preparation for the confocal microscopy. This was possible as the signal intensity in the cell area was incomparably high regarding the background intensity of the medium. Moreover, the area inside the cell was selected as the region of interest (ROI) for the lifetime determination in the obtained FLIM pictures allowing to exclude the background signal from the analysis.

2.9. Fluorescence lifetime imaging microscopy (FLIM)

Fluorescence lifetime images were acquired using a fluorescence lifetime microscope MicroTime-200 (PicoQuant, Germany) coupled to the inverted microscope Olympus IX-71 (Olympus, Japan). FLIM with a 100 \times oil objective having NA 1.4 enabled a minimum spatial resolution of 300 nm and a maximum scan area of 80 μ m \times 80 μ m. The pulsed laser diode LDH-P-C483 (PicoQuant, Germany) emitting at 483 nm (time resolution 120 ps) was used for fluorescence excitation and the emission was monitored using 510 nm long pass filter. The cells also were imaged with IDS uEye camera coupled to microscope. The SymPhoTime 64 software was used to calculate the lifetime map images. During imaging the living PC-3 cells were kept at 37 °C and at 5% CO₂ using an objective heater (Bioscience Tools, California, USA, TC-1-1005 Temperature Controller) and a custom-made incubator. In FLIM images the colors are based on the mean intensity weighted lifetimes $\langle \tau \rangle = (\sum_i I_i \tau_i) / (\sum_i I_i)$ at each pixel. To gain more information on the lifetime changes, a region of interest (ROI) was selected and the corresponding fluorescence decay was extracted. The fluorescence decay curves were fitted by applying iterative least-squares method to the sum of exponents in the equation $I(t, \lambda) = \sum_i a_i(\lambda) e^{-t/\tau_i}$ where τ_i is the lifetime and $a_i(\lambda)$ is the amplitude (pre-exponential factor) and the amplitude weighted average fluorescence lifetimes were calculated as $\langle \tau \rangle = (\sum_i a_i \tau_i) / (\sum_i a_i)$ (more about these two averaged lifetimes in SI Fig. S2) [42].

In each imaging series multiple cells were followed and the total number of imaged cells were 10 for Ptx-OG-20 K MVs and Ptx-OG-110 K EXOs and 9 for free Ptx-OG. The fluorescence lifetimes τ_1 and τ_2 at each time point (Fig. 4) are arithmetic means of the values calculated from several cells. The error bars represent range error bars obtained as $\tau_i^{max} - \tau_i^{min}$, where τ_i^{max} and τ_i^{min} are maximal and minimal lifetime values at about the same time point i , respectively [62].

2.10. Confocal microscopy

The confocal microscopy studies were performed for the validation and as a comparison for the FLIM studies. Ptx-OG trafficking to living PC-3 cells as bound to EVs was explored using Leica SP5 HCS confocal microscope (Leica, Germany) equipped with Leica DMI6000 B microscope and DPSS 561 nm/20 mW, Argon 488 nm/45 mW and HeNe 633 nm/12 mW lasers were used for fluorescence excitation and a

Table 1

Fluorescence lifetimes, τ_i , and in the case of two-exponential fluorescence decay the proportion of the shorter-living component, a_2 , for Ptx-OG in different systems.

Solution and hydrogel samples	τ_1 (ns)	τ_2 (ns)	a_2 (%)
Free Ptx-OG in DPBS (pH = 7.0)	4.4	–	–
Ptx-OG-EVs (both 20 K MVs and 110 K EXOs) in DPBS (pH = 7.0)	4.0	–	–
Free Ptx-OG in NFC hydrogel in water	4.1	1.9	36
Ptx-OG-20 K MVs in NFC hydrogel in water	4.0	1.9	34
Ptx-OG-20 K MVs in NFC hydrogel + Triton X in water	4.3	1.9	21
Ptx-OG-110 K EXOs in NFC hydrogel in water	3.9	1.9	32
Ptx-OG-110 K EXOs in NFC hydrogel + Triton X in water	4.1	2.1	20

single-photon avalanche detector (SPAD) and hybrid detector (HyD) used to detect the fluorescence. 45,000 PC-3 cells were inoculated in each well of a glass bottom 24-well plate (MatTek, Ashland Massachusetts, USA). The cell membranes and lysosomes were labeled for imaging at ~70% confluency. In order to demonstrate the co-localization and release of Ptx-OG from the EVs uptaken by the cells, MVs were labeled with lipophilic DiD label and loaded with Ptx-OG, and imaged using confocal microscopy.

The cell membranes were labeled with CellMask Deep Red Plasma membrane label. The stock solution of the membrane label was diluted to cell culture medium in 1:1000, and 50 μ l of the dilution was added to the wells. The lysosomes and endosomes of the PC-3 cells were labeled with LysoTracker Red (Invitrogen, California, USA) using a dilution of 1:1000 in culture medium and 50 μ l of the dilution was added to the wells. The cells were incubated with membrane and lysosome labels simultaneously for 60 min at 37 °C. After the incubation, the culture medium was carefully aspirated and the wells were washed 2–3 times with 0.5 ml of pre-heated culture medium. Lastly, either 400 μ l of plain culture medium, or 110 K EXOs or 20 K MVs suspended in culture medium were added to the cells.

All confocal images were acquired using 20 \times objective and Leica HCS A Matrix Screener software (Leica Microsystems, Germany) that recorded images from the wells every 2 h over the 22 h observation period. Every well was imaged at four different positions from 0 to 22 h, and from 24 to 42 h after adding the EVs. LysoTracker Red was excited using 581 nm wavelength, CellMask Deep Red Plasma (CM, cell membranes) or DiD (alternative membrane label) using 633 nm, and Ptx-OG using 488 nm. The cells were kept at 5% CO₂ and 37 °C during the imaging.

2D images were analyzed with Fiji software (an open source image processing package based on ImageJ) to create 3D renditions of the cells. The 3D images were processed with Imaris 7.7.2 software (Bitplane AG, Switzerland). Briefly, in the 3D analysis the cells were defined by formulating a surface using the CM channel, and the lysosomes with the LR channel. In the next stage, the average intensity of Ptx-OG inside cells or lysosomes was calculated for each sample as a function of time. As four locations were imaged in every well, an average of the four sectors was calculated. In order to follow the release of Ptx-OG from the microvesicles, a separate surface was defined for DiD used to label microvesicles.

3. Results

Our model system comprised of prostate cancer cells (PC-3) and their autologous EVs loaded with Ptx-OG. The EVs were characterized using Western blot analysis and nanoparticle tracking analysis as described in our earlier studies [30, 35]. The EVs were found to migrate to iodixanol fractions in the range of 1.058–1.163 g/ml, which corresponds to the density reported by others as well [63, 64]. While 20 K MVs were found to be slightly larger on average, the size distributions

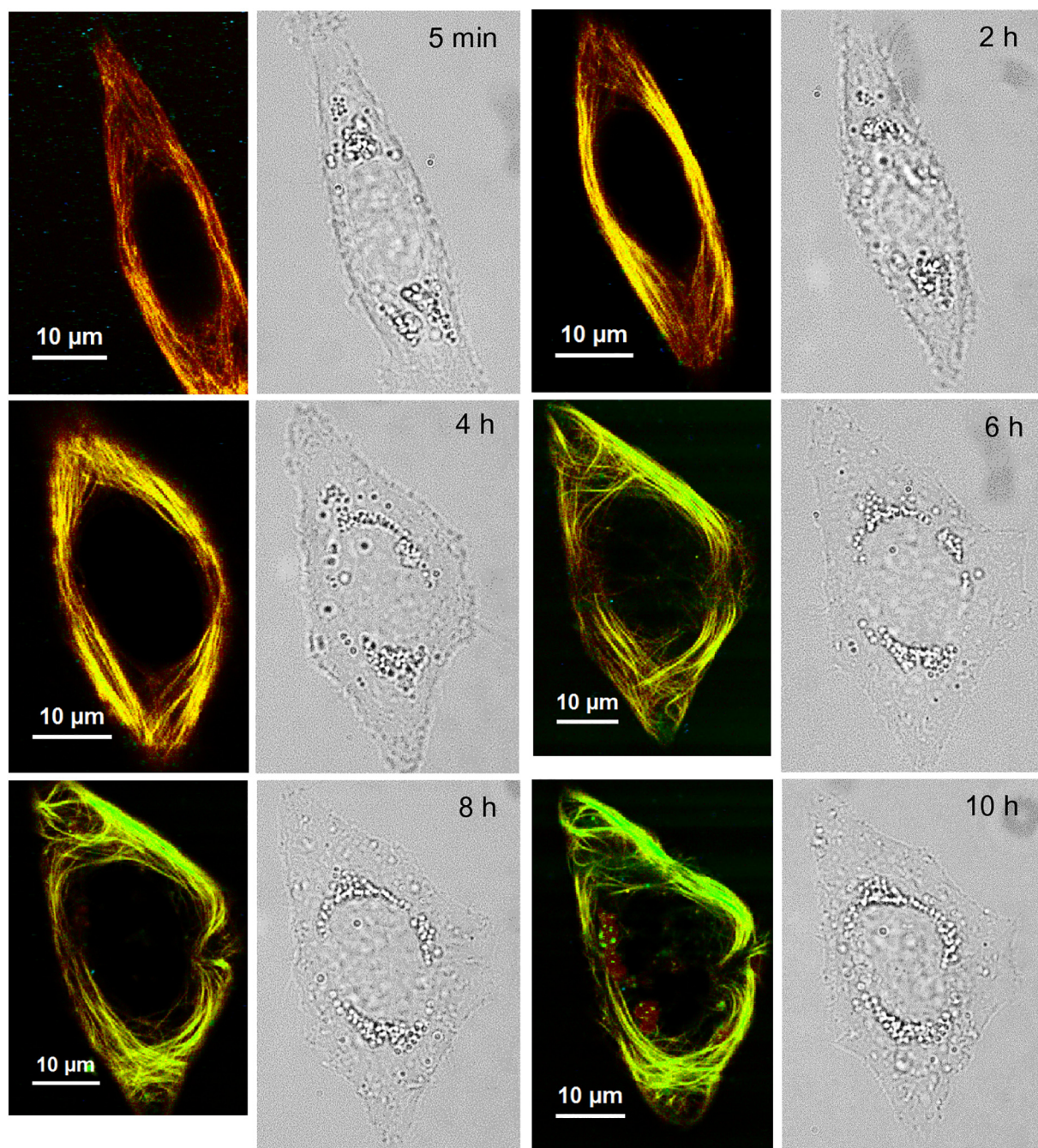



Fig. 1. FLIM and light microscope images of the PC-3 cells at different times after the addition of free Ptx-OG. The brightness of each pixel in the FLIM images correlates with the concentration of the fluorescent species in the corresponding spatial location. The color of each pixel in the FLIM images correlates with the average fluorescence lifetime in the corresponding spatial location as follows: 2.0 ns  4.5 ns.

analyzed by NTA showed heavy overlapping between 20 K MV and 110 K EXO populations, with the mode diameter being approximately 200 nm in both (SI Fig. S3A). Therefore we conclude no meaningful difference in the size profiles of 20 K MVs and 110 K EXOs. Western blot analysis of TSG101 and Hsp70 showed that TSG101 appeared to be slightly enriched in both EV populations compared to the cell lysate, while Hsp70 is found significantly more in the cells (SI Fig. S3B). 110 K EXO and 20 K MV populations seemed to express these two proteins at a similar level. Taken together these results regarding the density, size and TSG101 enrichment suggest the presence of EVs in our preparations, and that 20 K MVs and 110 K EXOs were very similar despite their differences in sedimentation speeds. However, total protein concentration per vesicle for 110 K EXOs was 2–4 times higher than that for

20 K MVs, suggesting a clear difference in protein content of the studied EV populations (SI Fig. S3C).

3.1. Ptx-OG fluorescence lifetimes in different environments

To be able to interpret the changes in OG fluorescence lifetime during EV uptake and their intracellular trafficking, we measured the fluorescence lifetimes of Ptx-OG in different systems (Table 1, SI Fig. S4). In solution, the fluorescence of Ptx-OG and Ptx-OG labeled EVs was one-exponential with lifetimes of 4.4 ns and 4.0 ns, respectively. To be able to simulate Ptx-OG fluorescence lifetimes in a system, which resembles the free physical situation when EVs are either on the cell surface or in the cytosol, we made the same measurements in 1.5% of

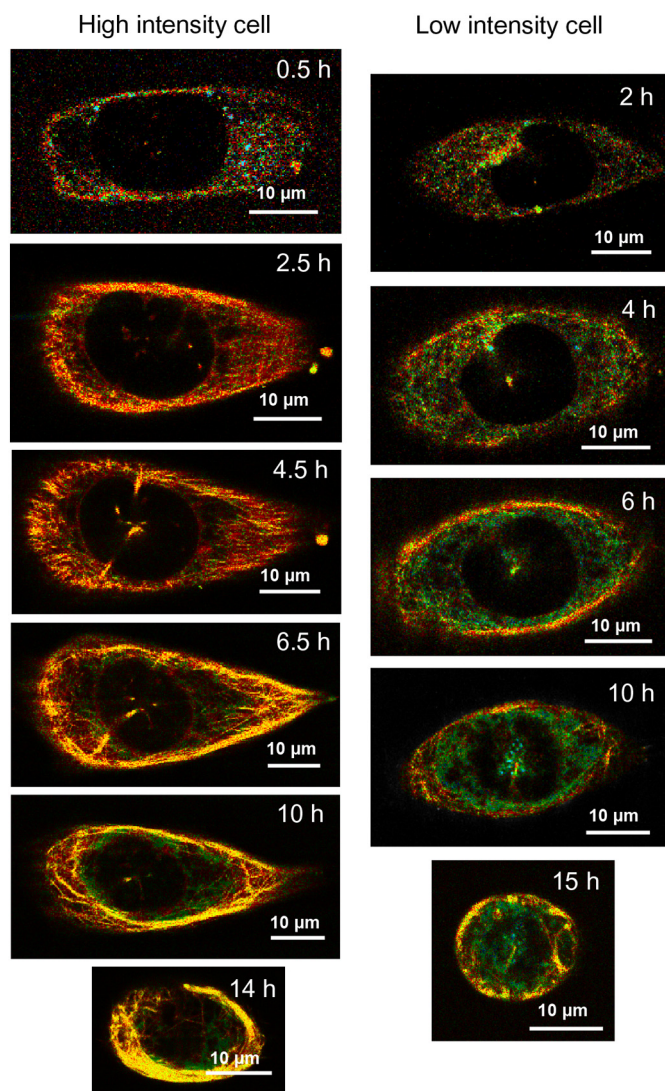


Fig. 2. FLIM images of the PC-3 cells (high intensity cell on the left and low intensity cell on the right) at different times after the addition of Ptx-OG loaded 20 K MVs. The brightness of each pixel in the FLIM images correlates with the concentration of the fluorescent species in the corresponding spatial location. The color of each pixel in the FLIM images correlates with the average fluorescence lifetime in the corresponding spatial location as follows: 2.0 ns (red) to 4.5 ns (blue).

nanofibrillar cellulose (NFC) hydrogel in water. It is now known, that NFC hydrogel interaction with EVs is only mechanical and no chemical interaction is present (data under submission). For free Ptx-OG and EV bound Ptx-OG in NFC hydrogel the fluorescence decays were 2-exponential and the proportion of the shorter, about 1.9 ns, component was about 34%. The lifetime of the longer living component was about 4.0 ns, corresponding to that of free Ptx-OG and Ptx-OG-EVs in solution. The change from one-exponential decay in solution to two-exponential in NFC hydrogel was probably a result of partial aggregation of Ptx-OG molecules or Ptx-OG-EVs due to the higher viscosity of the environment [65] and thus reflects the behavior of Ptx-OG, EV-bound or free, gathering to certain sites inside the cell. When Ptx-OG was released from the EVs by a Triton X treatment (Table 1, SI Fig. S4), the proportion of the shorter decay component decreased to about 20% indicating that the environment of Ptx-OG changes closer to that in solution.

3.2. FLIM reveals differences in cellular uptake mechanisms and functions between 110 K EXO and 20 K MV populations

3.2.1. Free Ptx-OG

FLIM images for the free Ptx-OG taken at various time points and the corresponding light microscope images are presented in Fig. 1. As a hydrophobic molecule, free Ptx-OG gathers very efficiently to the cell membrane: already 5 min after adding Ptx-OG to the medium, some cells showed intense Ptx-OG fluorescence (Fig. 1, red color, $\langle \tau \rangle_1 = 4.0$ ns). After passing through the cell membrane, Ptx-OG accumulated to the microtubules of the cell (yellow color). Between 6 and 12 h after adding Ptx-OG to the medium the average fluorescence lifetime $\langle \tau \rangle_1$ decreased slightly from 3.9 ns to 3.6 ns (from yellow to green) reflecting the changes taking place in the Ptx-OG environment.

3.2.2. Microvesicles

FLIM images for Ptx-OG at different time points are presented in Fig. 2. Two different types of cell behavior were observed in all samples. For some cells, the 20 K MV up-take was more efficient leading to higher fluorescence intensities (Fig. 2, high intensity cells). Due to slow diffusion of Ptx-OG-20 K MVs through the medium, the fluorescence in the cells was rather weak still at 1 h after Ptx-OG-20 K MV addition to the medium. At this point $\langle \tau \rangle_1$ was 3.9 ns. At 2.5 h, the high intensity cells showed intense red color of Ptx-OG-20 K MVs accumulated onto the cell membrane. At 4.5 h the fluorescence intensity had doubled and part of the Ptx-OG had already accumulated to the microtubules (yellow color). At about 6 h after Ptx-OG-20 K MV addition, a change was observed: a second fluorescent area with shorter fluorescence lifetime (green color) started to emerge around the nucleus. In time, the intensity of Ptx-OG fluorescence increased, and ca. 14 h after 20 K MV addition the cells started to round and die.

For other cells, the low intensity cells, the 20 K MV up-take seemed to be weaker: the fluorescence intensity stayed much (at least 4 times) lower than in the high intensity cells and smaller part of Ptx-OG gathered slowly to microtubules (orange and yellow color). The rest of Ptx-OG spread unevenly to the cytosol (green color), probably attached to any available membrane structures such as the endosomal network. At about 10 h, the borders of the nucleus started to fade and the cells started to die. For both types of cells, a fluorescent spot started to form in the middle of the dark area i.e. close to nucleus surface. It was not completely isolated from the other fluorescing areas and its $\langle \tau \rangle_1$ was equal to that in the microtubules (yellow color). Thus, it probably belongs to the microtubules network and could also be the centrosome.

3.2.3. Exosomes

FLIM images for the Ptx-OG (OG) are presented in the Fig. 3. In contrast to MVs, all the cells behaved more or less similarly when in contact with 110 K EXOs. At 1 h after addition of 110 K EXOs, they had spread to the cell membrane and Ptx-OG was partially internalized. A distribution of different fluorescence lifetimes (colors) was observed reflecting the different phases of this process. The 110 K EXOs can either fuse with the endosome membrane releasing Ptx-OG to the cytosol or end up degraded in the lysosomes. Again, as in the case of 20 K MVs, the released Ptx-OG gathered to microtubules (yellow color) and membrane structures such as the endosomal network (green color). As in the case of 20 K MVs, in most cells a yellow fluorescent spot started to form in the middle of the nucleus. After about 10 h the cells start to round and die.

3.3. Fluorescence lifetime analysis

In the cells, the fluorescence decays of Ptx-OG were two-exponential for all the studied delivery systems. The amplitude ratios of the two components, τ_1 and τ_2 , stayed almost constant between 25 and 35% for free Ptx-OG and Ptx-OG-20 K MVs. For the Ptx-OG-110 K EXOs, the ratio of the shorter-living component decreased from 45% to 30% in the

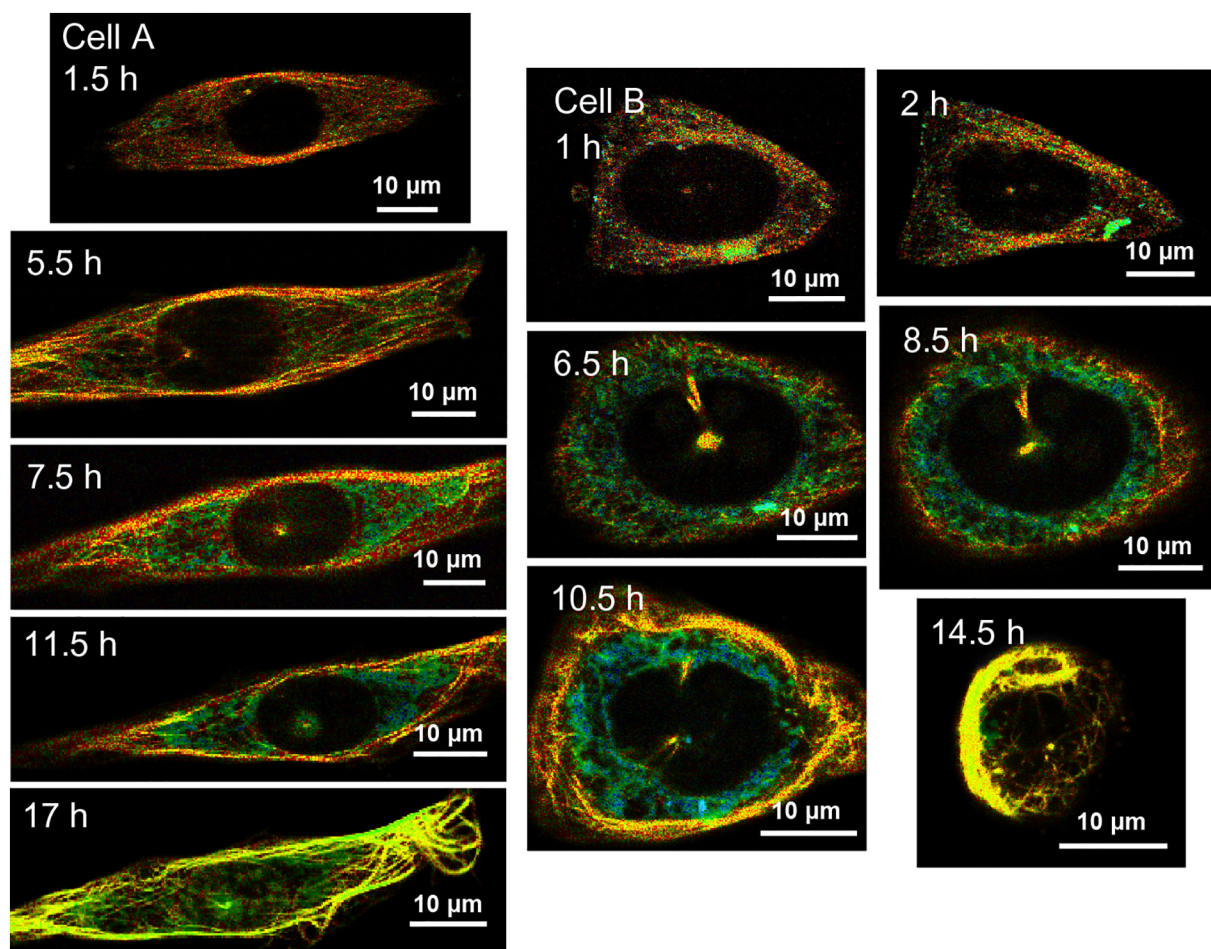



Fig. 3. FLIM images of two PC-3 cells (cells A and B) at different times after the addition of Ptx-OG loaded 110 K EXOs. The brightness of each pixel in the FLIM images correlates with the concentration of the fluorescent species in the corresponding spatial location. The color of each pixel in the FLIM images correlates with the average fluorescence lifetime in the corresponding spatial location as follows: 2.0 ns  4.5 ns.

Table 2

Fluorescence lifetimes, τ_i , and in the case of two-exponential fluorescence decay the proportion of the shorter-living component, a_2 , and amplitude weighted average fluorescence lifetime, $\langle \tau \rangle_a$, for Ptx-OG in different systems.

Cell samples	Interaction time	τ_1 (ns)	τ_2 (ns)	a_2 (%)	$\langle \tau \rangle_a$
Free Ptx-OG in PC-3 cells ($N = 2$)	0–0.5 h	4.3	2.7	28	3.9
	12 h	4.0	1.9	32	3.3
Ptx-OG-20 K MVs in PC-3 HI-cells ($N = 3$)	3 h	4.3	2.3	25	3.8
	15 h	4.0	1.7	27	3.4
Ptx-OG-20 K MVs in PC-3 LI-cells ($N = 4$)	2.5 h	4.2	1.4	35	3.2
	16 h	4.0	1.5	34	3.1
Ptx-OG-110 K EXOs in PC-3 cells ($N = 4$)	2.5 h	4.1	1.2	44	2.8
	16 h	4.0	1.8	30	3.4

first 12 h (Table 2). In calculating the $\langle \tau \rangle_a$, these changes mostly cancel out each other. However, when looking at the behavior of the lifetime each decay component as a function of time (Fig. 4) clear trends were observed. The longer-living component τ_1 behaves similarly for all studied systems (Table 2 and Fig. 4a). During the first 2 h, while EVs gather to the cell membrane followed by uptake, τ_1 reached its maximal value of about 4.3 ns (Phase I, Fig. 4a). After this, during EV trafficking and functioning inside the cells, τ_1 decreased to 4.0 ns (Phase II, Fig. 4a) and stayed constant or slightly increased after 12 h during cell death (Phase III, Fig. 4a). For the shorter-living component τ_2 a clear difference between the different delivery systems was observed (Fig. 4b). For free Ptx-OG and Ptx-OG-MVs in high intensity cells, τ_2 behaved similarly decreasing from almost 3 ns to less than 2 ns during

the first 12 h (Phase I and II, Fig. 4b, squares and triangles). For Ptx-OG-110 K EXOs and Ptx-OG-20 K MVs in low intensity cells, τ_2 was nearly constant at about 1.2–1.5 ns for the first hours after cell uptake (Phase II, Fig. 4b, diamonds and inverted triangles). After 12 h τ_2 started to increase finally reaching 2.0 ns (Phase III, Fig. 4b, diamonds and inverted triangles). The τ_2 increase coincides to the signs of cell death in FLIM and light microscopy images and is assumed as an indication of cell collapse. Different cells of the low intensity cell subpopulation supplemented by Ptx-OG-20 K MVs died at different time points and most of them were dead after 18 h. This was seen by gradual increase in τ_2 at time range from 10 to 18 h (Fig. 4b, inverted triangles). In turn, 110 K EXO encapsulated Ptx-OG led to rather sharp increase in τ_2 between 12 and 15 h time points (Fig. 4b, diamonds) reflecting the faster and more simultaneous cell death compared to 20 K MV encapsulated drug. After 18 h, τ_2 became constant in all the systems corresponding to the cell death.

3.4. Confocal microscopy

In order to validate the FLIM approach, 110 K EXOs and 20 K MVs as drug carriers were examined using conventional confocal microscopy. Here CellMask Deep Red Plasma membrane label (excitation 633 nm) and LysoTracker Red (LR, lysosome label, excitation at 581) served as an alternative labels to acquire more in-depth comprehension on the EV-mediated drug delivery. The 3D confocal images of PC-3 cells incubated with Ptx-OG loaded 110 K EXOs and 20 K MVs are displayed in Fig. 5.

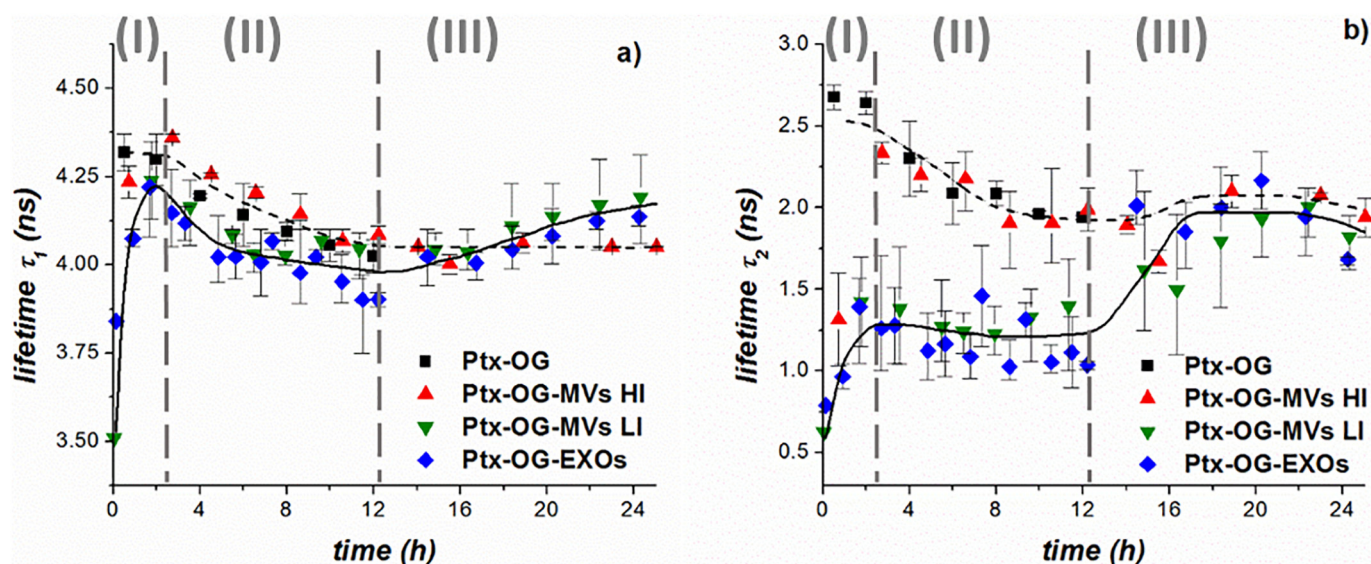


Fig. 4. Average fluorescence lifetimes a) τ_1 and b) τ_2 from two-exponential fits on the fluorescence decays obtained from the ROIs inside the cells in the FLIM images of PC-3 cells as a function of time after addition of Ptx-OG (squares), Ptx-OG-EV (Ptx-OG-110 K EXOs – diamonds, Ptx-OG-20 K MVs – triangles for high intensity HI cells and inverted triangles for low intensity LI cells) with range error bars. The solid lines indicate the behavior when endocytosis is suggested as main mechanism of EV uptake and dashed line indicates the behavior when plasma membrane fusion of EVs or direct interaction of pure Ptx-OG with the membrane is suggested as the main uptake mechanism. Three clear phases for behavior of the lifetimes were visible and are separated by vertical dashed lines: (I) EV gathering around the cells and interaction with membrane followed by uptake (II) Intracellular EV trafficking and functioning, and (III) Cell death.

Consistent with the FLIM results, we perceived that Ptx-OG loaded into the EV carriers interacted with and was internalized into the PC-3 cells already after 2–3 h of adding the 110 K EXOs or 20 K MVs. Several, but not all cells' microtubules were labeled until they died at ~20 h; this phenomenon has been reported in our previous study [35]. Intriguingly, the confocal images on 20 K MVs demonstrated that Ptx-OG was distributed more evenly on the membranes of PC-3 cells than 110 K EXOs that exhibited spot-resembling distribution of Ptx-OG. This indicates that MVs use primarily plasma membrane fusion mechanism during the internalization whereas the main uptake mechanism for 110 K EXOs could be endosomal route. However, for both 110 K EXOs and 20 K MVs some Ptx-OG fluorescence appeared to reside at the same locations where LR exposed the lysosomes. These perceptions indicate the existence of multiple overlapping cellular uptake mechanisms. Although 20 K MVs mainly released Ptx-OG through the membrane fusion, a proportion of them were apparently internalized via endocytic pathways as they were seen to accumulate into the lysosomes. The merged representation and differential interference contrast (DIC) images finally illustrated the overall sequence of events showing that the morphology of PC-3 cells changed towards circular-shaped and intumescent. Finally, at the 42 h observation point all the examined cells were dead.

4. Discussion

To elucidate the above presented results, the possible fates of Ptx during the studied drug delivery processes is discussed taking into account the known pharmacological mechanism of Ptx presented in the introduction. Three phases can be recognized from the different fluorescence lifetimes (Fig. 4) at specific localizations in the cell observed in FLIM and the confocal microscopy results (Fig. 5). In phase I (0–2 h) the EVs gather around the cells and interact with plasma membrane followed by uptake – red color appears in FLIM images. In phase II (2–12 h) EV trafficking and functioning takes place inside the cells – yellow and green colors in FLIM images depending on the EV location in the cell. In phase III (after 12 h) the cell death takes place – greenish yellow color in FLIM images and clear morphology changes in the cells. In order to label the microtubules, at least a proportion of Ptx-OG has to

be liberated from the 110 K EXO/20 K MV carrier whilst the internalization is ongoing. Since we observed microtubules network labeling by Ptx-OG already after ~5 h of initiating the incubation of PC-3 cells with 110 K EXOs/20 K MVs (Figs. 2 and 3, yellow color), we hypothesize that some amount of Ptx-OG diffuses out from the carriers almost immediately at the beginning of PC-3 cell uptake. For Ptx-OG-20 K MVs in PC-3 high intensity cells, the staining pattern at ~5 h resembles that of free Ptx-OG suggesting that in high intensity cells direct fusion of 20 K MVs with the plasma membrane may dominate over endocytosis. Leaking of Ptx from the EVs could be another interpretation for the observed result. However, in our earlier studies no significant leakage of Ptx from Ptx-EVs was detected after 24 and 48 h incubation at 37 °C [35]. Interestingly, for 20 K MV carriers not all the microtubules were labeled simultaneously, which might reflect paclitaxel's cell cycle specificity or multiple functions [66, 67]. Besides microtubules, Ptx can also bind to an apoptosis-regulator protein called Bcl-2, inhibiting its function, which can lead to apoptosis as well [66]. Bcl-2 is typically found in the membranes of the nuclear envelope, endoplasmic reticulum and mitochondria [68]. For Ptx-OG-110 K EXOs, once Ptx-OG has been released from the 110 K EXOs to the cytosol, only part of it accumulates onto microtubules (yellow color). The main part of Ptx-OG delivered by 110 K EXOs shows shorter fluorescence lifetime (green color) indicating that it has bound to another cellular target which could be the apoptosis regulator Bcl-2, given that these cells die with significantly different staining patterns compared to free Ptx-OG that clearly stains microtubules. At about 12 h the morphology of the cells start to change and the Ptx-OG fluorescence lifetime increases. This could indicate the onset of apoptosis and the release of Ptx-OG from Bcl-2. Taken together, the observations at (5–17 h) indicate that Ptx-OG has been released from their 110 K EXO carriers and acting as expected, initiates interaction with the microtubules network and/or with Bcl-2, which ultimately leads to cell death [69, 70].

There is always some overlap on the size distributions of 110 K EXOs and 20 K MVs and thus neither of these two up-take mechanisms for Ptx-OG action can be completely ruled out for either of the carriers, but exist in parallel. This is very clearly observed for 20 K MVs in PC-3 low intensity cells: Ptx-OG acts very similarly to the 110 K EXO delivered Ptx-OG. For 110 K EXOs in part of the cells (cell A in Fig. 3) fast

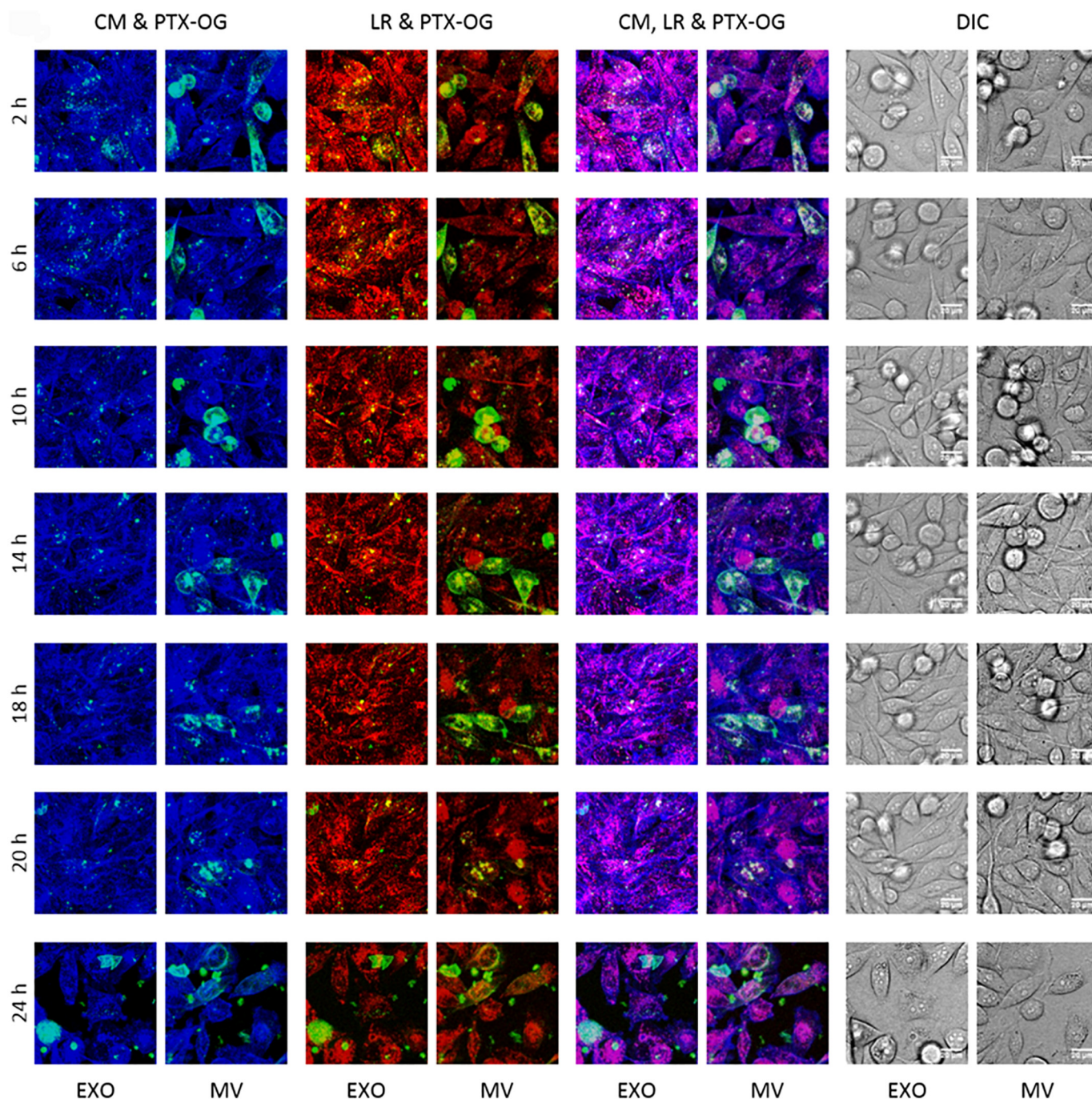


Fig. 5. Confocal microscopic analysis of EV-mediated Ptx-OG delivery. Picture panel with 3D rendered confocal microscopy images of EV-mediated Ptx-OG delivery process into PC-3 cells. PC-3 cells were treated with Ptx-OG carrying EVs, imaged using confocal microscopy every 2 h, and the localization of Ptx-OG inside the cells and lysosomes was quantified using 3D analysis. Channels from left to right; cells labeled with CellMask Deep Red Plasma membrane label (CM, blue) with Ptx-OG (green) loaded MVs or EXOs (CM & Ptx-OG), PC-3 cells' lysosomes labeled with LysoTracker Red (LR, red) and Ptx-OG loaded MVs or EXOs (LR & Ptx-OG), merge of CM, LR & Ptx-OG channels (CM, LR & Ptx-OG), differential interference contrast (DIC) microscopy images. (For interpretation of the references to color in this figure legend, the reader is referred to the web version of this article.)

accumulation to microtubules takes place. This could mean that part of the 110 K EXOs fuse with the cell membrane and release Ptx-OG directly to the cytosol.

At the moment, the sub-cellular mechanism of Ptx induced cell death remains partly speculative. More measurements with the Ptx targets labeled with suitable fluorescent probes would be needed to confirm the suggested scheme of events. However, the data presented in here already shows us, that the two overlapping mechanisms of Ptx induced cell death can be identified by FLIM studies and that the main

route depends on whether Ptx is administered via 110 K EXOs or 20 K MVs.

5. Conclusions

Herein, we have demonstrated that FLIM is an effective method to follow the EV-mediated drug delivery on intracellular level. Our data illustrates that the internalization pathways of 110 K EXOs and 20 K MVs are different and can be distinguished with this method. Subtle

sub-cellular mechanisms of EV movements and the release of Ptx-OG from EVs can be predicted by harnessing the changes in the excited state lifetime of a fluorescent probe, which is sensitive to physical and chemical changes in its microenvironment. All this information was obtained from a single fluorescing species since instead of fluorescence intensity fluorescence lifetime was used to analyze the data. Hence, we envisage that FLIM provides a completely new method to obtain in-depth insights into these aspects, and the obtained results may inspire the experts in the EV field to discover other prospective uses for FLIM.

Acknowledgements

Orion Foundation is acknowledged by M.Y.; Tekes – Finnish Center for Innovation is acknowledged by T.R., H.S., L.N. O.-P. N.; Kordelin Foundation is acknowledged by H.S.; CIMO Winter School is acknowledged by E.L., Academy of Finland (311362 and 258114) is acknowledged by T.L, K.R., E.L., E.V.-L.

Author contributions

All the authors participated in planning the experiments and analyzing the data. Experiments were performed by H.S., E.L. K.R., L.N. and O.-P. N. Writing of the manuscript was performed by H.S., E.L., K.R., T.R., M.Y. and E.V.-L. All the authors actively participated in commenting and editing to finalize the manuscript.

Appendix A. Supplementary data

Supplementary data to this article can be found online at <https://doi.org/10.1016/j.jconrel.2018.06.015>.

References

- [1] M. Colombo, G. Raposo, C. Théry, Biogenesis, secretion, and intercellular interactions of exosomes and other extracellular vesicles, *Annu. Rev. Cell Dev. Biol.* 30 (2014) 255–289.
- [2] G. Raposo, W. Stoorvogel, Extracellular vesicles: exosomes, microvesicles, and friends, *J. Cell Biol.* 200 (2013) 373–383.
- [3] B. György, T.G. Szabó, M. Pásztói, Z. Pál, P. Misják, B. Aradi, V. László, É. Pállinger, E. Pap, Á. Kittel, G. Nagy, A. Falus, E.I. Buzás, Membrane vesicles, current state-of-the-art: emerging role of extracellular vesicles, *Cell. Mol. Life Sci.* 68 (2011) 2667–2688.
- [4] M.I. Ramirez, M.G. Amorim, C. Gadelha, I. Milic, J.A. Welsh, V.M. Freitas, M. Nawaz, N. Akbar, Y. Couch, L. Makin, F. Cooke, A.L. Vettore, P.X. Batista, R. Freezor, J.A. Pezuk, L. Rosa-Fernandes, A.C.O. Carreira, A. Devitt, L. Jacobs, I.T. Silva, G. Coakley, D.N. Nunes, D. Carter, G. Palmisano, E. Dias-Neto, Technical challenges of working with extracellular vesicles, *Nano* 10 (2018) 881–906.
- [5] J.P.K. Armstrong, M.N. Holme, M.M. Stevens, Europe PMC Funders Group Re-Engineering Extracellular Vesicles as Smart Nanoscale Therapeutics Extracellular Vesicles: Cell-Derived Nanovectors Europe PMC Funders Author Manuscripts, 11 (2017), pp. 69–83, <http://dx.doi.org/10.1021/acsnano.6b07607>. Re-Engineering.
- [6] S. El Andaloussi, I. Mäger, X.O. Breakefield, M.J.A. Wood, Extracellular vesicles: biology and emerging therapeutic opportunities, *Nat. Rev. Drug Discov.* 12 (2013) 347–357.
- [7] C. Théry, M. Ostrowski, E. Segura, Membrane vesicles as conveyors of immune responses, *Nat. Rev. Immunol.* 9 (2009) 581–593.
- [8] P.D. Robbins, A.E. Morelli, Regulation of immune responses by extracellular vesicles, *Nat. Rev. Immunol.* 14 (2014) 195–208.
- [9] K. Al-Nedawi, B. Meehan, J. Micallef, V. Lhotak, L. May, A. Guha, J. Rak, Intercellular transfer of the oncogenic receptor EGFRvIII by microvesicles derived from tumour cells, *Nat. Cell Biol.* 10 (2008) 619–624.
- [10] J. Skog, T. Würdinger, S. van Rijn, D.H. Meijer, L. Gainche, W.T. Curry, B.S. Carter, A.M. Krichevsky, X.O. Breakefield, Glioblastoma microvesicles transport RNA and proteins that promote tumour growth and provide diagnostic biomarkers, *Nat. Cell Biol.* 10 (2008) 1470–1476.
- [11] D.G. Meckes, K.H.Y. Shair, A.R. Marquitz, C.-P. Kung, R.H. Edwards, N. Raab-Traub, Human tumor virus utilizes exosomes for intercellular communication, *Proc. Natl. Acad. Sci. U. S. A.* 107 (2010) 20370–20375.
- [12] L. Balaj, R. Lessard, L. Dai, Y.-J. Cho, S.L. Pomeroy, X.O. Breakefield, J. Skog, Tumour microvesicles contain retrotransposon elements and amplified oncogene sequences, *Nat. Commun.* 2 (2011) 180.
- [13] M.A. Antonyak, B. Li, L.K. Boroughs, J.L. Johnson, J.E. Druso, K.L. Bryant, D.A. Holowka, R.A. Cerione, Cancer cell-derived microvesicles induce transformation by transferring tissue transglutaminase and fibronectin to recipient cells, *Proc. Natl. Acad. Sci.* 108 (2011) 4852–4857.
- [14] G. Fuhrmann, A.L. Neuer, I.K. Herrmann, Extracellular vesicles – a promising avenue for the detection and treatment of infectious diseases? *Eur. J. Pharm. Biopharm.* 118 (2017) 56–61.
- [15] J.S. Schorey, C.V. Harding, Extracellular vesicles and infectious diseases: new complexity to an old story, 126 (2016), pp. 1181–1189.
- [16] W. Zhang, X. Jiang, J. Bao, Y. Wang, H. Liu, L. Tang, Exosomes in pathogen infections: a bridge to deliver molecules and link functions, *Front. Immunol.* 9 (2018) 1–12, <http://dx.doi.org/10.3389/fimmu.2018.00090>.
- [17] E.I. Buzas, B. György, G. Nagy, A. Falus, S. Gay, Emerging role of extracellular vesicles in inflammatory diseases, *Nat. Rev. Rheumatol.* 10 (2014) 356–364.
- [18] T. Garg, A.K. Goyal, Liposomes: targeted and controlled delivery system, *Drug Deliv. Lett.* 4 (2014) 62–71 <http://www.ingentaconnect.com/content/ben/ddl/2014/00000004/00000001/art00008>.
- [19] A. Hoshino, B. Costa-Silva, T.-L. Shen, G. Rodrigues, A. Hashimoto, M. Tesic Mark, H. Molina, S. Kohsaka, A. Di Giannatale, S. Ceder, S. Singh, C. Williams, N. Soplop, K. Uryu, L. Pharmed, T. King, L. Bojmar, A.E. Davies, Y. Ararso, T. Zhang, H. Zhang, J. Hernandez, J.M. Weiss, V.D. Dumont-Cole, K. Kramer, L.H. Wexler, A. Narendran, G.K. Schwartz, J.H. Healey, P. Sandstrom, K. Jørgen Labori, E.H. Kure, P.M. Grandgenett, M.A. Hollingsworth, M. de Sousa, S. Kaur, M. Jain, K. Mallya, S.K. Batra, W.R. Jarnagin, M.S. Brady, O. Fodstad, V. Muller, K. Pantel, A.J. Minn, M.J. Bissell, B.A. Garcia, Y. Kang, V.K. Rajasekhar, C.M. Ghajar, I. Matei, H. Peinado, J. Bromberg, D. Lyden, Tumour exosome integrins determine organotropic metastasis, *Nature* 527 (2015) 329–335.
- [20] S.C. Jang, O.Y. Kim, C.M. Yoon, D.-S. Choi, T.-Y. Roh, J. Park, J. Nilsson, J. Lötvall, Y.-K. Kim, Y.S. Gho, Bioinspired exosome-mimetic nanovesicles for targeted delivery of chemotherapeutics to malignant tumors, *ACS Nano* 7 (2013) 7698–7710.
- [21] E.V. Batrakova, M.S. Kim, Using exosomes, naturally-equipped nanocarriers, for drug delivery, *J. Control. Release* 219 (2015) 396–405.
- [22] P. Vader, E.A. Mol, G. Pasterkamp, R.M. Schiffelers, Extracellular vesicles for drug delivery, *Adv. Drug Deliv. Rev.* 106 (2016) 148–156.
- [23] C. Subra, K. Laulagnier, B. Perret, M. Record, Exosome lipidomics unravels lipid sorting at the level of multivesicular bodies, *Biochimie* 89 (2007) 205–212.
- [24] D.S. Choi, J.M. Lee, G.W. Park, H.W. Lim, J.Y. Bang, Y.K. Kim, K.H. Kwon, H.J. Kwon, K.P. Kim, Y.S. Gho, Proteomic analysis of microvesicles derived from human colorectal cancer cells, *J. Proteome Res.* 6 (2007) 4646–4655.
- [25] S. Sharma, B.M. Gillespie, V. Palanisamy, J.K. Gimzewski, Quantitative nanostructural and single-molecule force spectroscopy biomolecular analysis of human saliva-derived exosomes, *Langmuir* 27 (2011) 14394–14400.
- [26] R.P. Carney, S. Hazari, T. Rojalin, A. Knudson, T. Gao, Y. Tang, R. Liu, T. Viitala, M. Yliperttula, K.S. Lam, Targeting tumor-associated exosomes with integrin-binding peptides, *Adv. Biosyst.* 1 (2017) 1–12, <http://dx.doi.org/10.1002/adbi.201600038>.
- [27] E.J. van der Vlist, E.N.M. Nolte-T Hoen, W. Stoorvogel, G.J.A. Arkesteijn, M.H.M. Wauben, Fluorescent labeling of nano-sized vesicles released by cells and subsequent quantitative and qualitative analysis by high-resolution flow cytometry, *Nat. Protoc.* 7 (2012) 1311–1326.
- [28] M.C. Henderson, D.O. Azorsa, The genomic and proteomic content of cancer cell-derived exosomes, *Front. Oncol.* 2 (2012) 1–38, <http://dx.doi.org/10.3389/fonc.2012.00038>.
- [29] G. Hu, K.M. Drescher, X.-M. Chen, Exosomal miRNAs: biological properties and therapeutic potential, *Front. Genet.* 3 (2012) 1–9, <http://dx.doi.org/10.3389/fgenet.2012.00056>.
- [30] Z.J. Smith, C. Lee, T. Rojalin, R.P. Carney, S. Hazari, A. Knudson, K. Lam, H. Saari, E.L. Ibañez, T. Viitala, T. Laaksonen, M. Yliperttula, S. Wachsmann-Hogiu, Single exosome study reveals subpopulations distributed among cell lines with variability related to membrane content, *J. Extracell. Vesicles.* 4 (2015) 1–15, <http://dx.doi.org/10.3402/jev.v4.28533>.
- [31] L. Grasso, R. Wyss, L. Weidenauer, A. Thampi, D. Demurtas, M. Prudent, N. Lion, H. Vogel, Molecular screening of cancer-derived exosomes by surface plasmon resonance spectroscopy, *Anal. Bioanal. Chem.* 407 (2015) 5425–5432.
- [32] D.L.M. Rupert, C. Lässer, M. Eldh, S. Block, V.P. Zhdanov, J.O. Lotvall, M. Bally, F. Höök, Determination of exosome concentration in solution using surface plasmon resonance spectroscopy, *Anal. Chem.* 86 (2014) 5929–5936.
- [33] T. Tian, Y. Wang, H. Wang, Z. Zhu, Z. Xiao, Visualizing of the cellular uptake and intracellular trafficking of exosomes by live-cell microscopy, *J. Cell. Biochem.* 111 (2010) 488–496.
- [34] S. Ohno, M. Takahashi, K. Sudo, S. Ueda, A. Ishikawa, N. Matsuyama, K. Fujita, T. Mizutani, T. Ohgi, T. Ochiya, N. Gotoh, M. Kuroda, Systemically injected exosomes targeted to EGFR deliver antitumor microRNA to breast cancer cells, *Mol. Ther.* 21 (2013) 185–191.
- [35] H. Saari, E. Lázaro-Ibañez, T. Viitala, E. Vuorimaa-Laukkanen, P. Siljander, M. Yliperttula, Microvesicle- and exosome-mediated drug delivery enhances the cytotoxicity of paclitaxel in autologous prostate cancer cells, *J. Control. Release* 220 (2015) 727–737.
- [36] K. Suhling, M.W. French, D. Phillips, Time-resolved fluorescence microscopy, *Photochem. Photobiol. Sci.* 4 (2005) 13–22.
- [37] M.Y. Berezin, S. Achilefu, Fluorescence lifetime measurements and biological imaging, *Chem. Rev.* 110 (2010) 2641–2684.
- [38] W. Becker, Fluorescence lifetime imaging-techniques and applications, *J. Microsc.* 247 (2012) 119–136.
- [39] H. Wallrabe, A. Periasamy, Imaging protein molecules using FRET and FLIM microscopy, *Curr. Opin. Biotechnol.* 16 (2005) 19–27.
- [40] J.W. Lichtman, J.-A. Conchello, Fluorescence microscopy, *Nat. Methods* 2 (2005) 910–919.
- [41] J.R. Lakowicz, Principles of Fluorescence Spectroscopy, 3rd ed., Springer Science + Business Media, LLC, New York, 2006.

- [42] B. Valeur, M.N. Berberan-Santos, *Molecular Fluorescence: Principles and Applications*, 2nd ed., Wiley-VCH, Weinheim, 2012.
- [43] M. Elangovan, R.N. Day, A. Periasamy, Nanosecond fluorescence resonance energy transfer-fluorescence lifetime imaging microscopy to localize the protein interactions in a single living cell, *J. Microsc.* 205 (2002) 3–14.
- [44] D. Dziuba, P. Jurkiewicz, M. Cebecauer, M. Hof, M. Hocek, A rotational BODIPY nucleotide: an environment-sensitive fluorescence-lifetime probe for DNA interactions and applications in live-cell microscopy, *Angew. Chem.* 128 (2016) 182–186.
- [45] C. Hille, M. Berg, L. Bressel, D. Munzke, P. Primus, H.-G. Löhmansröben, C. Dosche, Time-domain fluorescence lifetime imaging for intracellular pH sensing in living tissues, *Anal. Bioanal. Chem.* 391 (2008) 1871–1879.
- [46] M.K. Kuimova, Mapping viscosity in cells using molecular rotors, *Phys. Chem. Chem. Phys.* 14 (2012) 12671–12686.
- [47] M. Jose, D.K. Nair, C. Reissner, R. Hartig, W. Zschratler, Photophysics of Clomeleon by FLIM: discriminating excited state reactions along neuronal development, *Biophys. J.* 92 (2007) 2237–2254.
- [48] J. López-Gejo, D. Haigh, G. Orellana, Relationship between the microscopic and macroscopic world in optical oxygen sensing: a luminescence lifetime microscopy study, *Langmuir* 26 (2010) 2144–2150.
- [49] X. Dai, Z. Yue, M.E. Eccleston, J. Swartling, N.K.H. Slater, C.F. Kaminski, Fluorescence intensity and lifetime imaging of free and micellar-encapsulated doxorubicin in living cells, nanomedicine nanotechnology, *Biol. Med.* 4 (2008) 49–56.
- [50] G. Romero, Y. Qiu, R.A. Murray, S.E. Moya, Study of intracellular delivery of doxorubicin from poly(lactide-co-glycolide) nanoparticles by means of fluorescence lifetime imaging and confocal Raman microscopy, *Macromol. Biosci.* 13 (2013) 234–241.
- [51] J.S. Basuki, H.T.T. Duong, A. MacMillan, R.B. Erlich, L. Esser, M.C. Akerfeldt, R.M. Whan, M. Kavallaris, C. Boyer, T.P. Davis, Using fluorescence lifetime imaging microscopy to monitor theranostic nanoparticle uptake and intracellular doxorubicin release, *ACS Nano* 7 (2013) 10175–10189.
- [52] J.S. Lee, J. Feijen, Biodegradable polymersomes as carriers and release systems for paclitaxel using Oregon green® 488 labeled paclitaxel as a model compound, *J. Control. Release* 158 (2012) 312–318.
- [53] K. Tang, Y. Zhang, H. Zhang, P. Xu, J. Liu, J. Ma, M. Lv, D. Li, F. Katirai, G.-X. Shen, G. Zhang, Z.-H. Feng, D. Ye, B. Huang, Delivery of chemotherapeutic drugs in tumour cell-derived microparticles, *Nat. Commun.* 3 (2012) 1–11, <http://dx.doi.org/10.1038/ncomms2282>.
- [54] L. Pascucci, V. Coccè, A. Bonomi, D. Ami, P. Ceccarelli, E. Cusani, L. Viganò, A. Locatelli, F. Sisto, S.M. Doglia, E. Parati, M.E. Bernardo, M. Muraca, G. Alessandri, G. Bondiolotti, A. Pessina, Paclitaxel is incorporated by mesenchymal stromal cells and released in exosomes that inhibit in vitro tumor growth: a new approach for drug delivery, *J. Control. Release* 192 (2014) 262–270.
- [55] T. Yang, P. Martin, B. Fogarty, A. Brown, K. Schurman, R. Phipps, V.P. Yin, P. Lockman, S. Bai, Exosome delivered anticancer drugs across the blood-brain barrier for brain cancer therapy in Danio rerio, *Pharm. Res.* 32 (2015) 2003–2014.
- [56] D. Feng, W.-L. Zhao, Y.-Y. Ye, X.-C. Bai, R.-Q. Liu, L.-F. Chang, Q. Zhou, S.-F. Sui, Cellular internalization of exosomes occurs through phagocytosis, *Traffic* 11 (2010) 675–687.
- [57] I. Parolini, C. Federici, C. Raggi, L. Lugini, S. Palleschi, A. De Milito, C. Coscia, E. Iessi, M. Logozzi, A. Molinari, M. Colone, M. Tatti, M. Sargiacomo, S. Fais, Microenvironmental pH is a key factor for exosome traffic in tumor cells, *J. Biol. Chem.* 284 (2009) 34211–34222.
- [58] P.B. Schiff, J. Fant, S.B. Horwitz, Promotion of microtubule assembly in vitro by taxol, *Nature* 277 (1979) 665–667.
- [59] M.A. Jordan, R.J. Toso, D. Thrower, L. Wilson, Mechanism of mitotic block and inhibition of cell proliferation by taxol at low concentrations, *Proc. Natl. Acad. Sci. U. S. A.* 90 (1993) 9552–9556.
- [60] S.R. Elkin, A.M. Lakoduk, S.L. Schmid, Endocytic pathways and endosomal trafficking: a primer, *Wien. Med. Wochenschr.* 166 (2016) 196–204.
- [61] I. Prada, J. Meldolesi, Binding and fusion of extracellular vesicles to the plasma membrane of their cell targets, *Int. J. Mol. Sci.* 17 (2016) 1–8, <http://dx.doi.org/10.3390/ijms17081296>.
- [62] G. Cumming, F. Fidler, D.L. Vaux, Error bars in experimental biology, *J. Cell Biol.* 177 (2007) 7–11.
- [63] J. Van Deun, P. Mestdagh, R. Sormunen, V. Cocquyt, K. Vermaelen, J. Vandesompele, M. Bracke, O. De Wever, A. Hendrix, The impact of disparate isolation methods for extracellular vesicles on downstream RNA profiling, *J. Extracell. Vesicles.* 3 (2014) 1–14, <http://dx.doi.org/10.3402/jev.v3.24858>.
- [64] A. Cvjetkovic, S.C. Jang, B. Konečná, J.L. Höög, C. Sihlbom, C. Lässer, J. Lötvall, Detailed analysis of protein topology of extracellular vesicles—evidence of unconventional membrane protein orientation, *Sci. Rep.* 6 (2016) 1–12, <http://dx.doi.org/10.1038/srep36338>.
- [65] E.O. Puchkov, Intracellular viscosity: methods of measurement and role in metabolism, *Biochem. Suppl. Ser. A Membr. Cell Biol.* 7 (2013) 270–279.
- [66] C. Ferlini, L. Cicchillitti, G. Raspaglio, S. Bartollino, S. Cimitan, C. Bertucci, S. Mozzetti, D. Gallo, M. Persico, C. Fattorusso, G. Campiani, G. Scambia, Paclitaxel directly binds to Bcl-2 and functionally mimics activity of n77, *Cancer Res.* 69 (2009) 6906–6914.
- [67] P.-C. Liao, C.-H. Lieu, Cell cycle specific induction of apoptosis and necrosis by paclitaxel in the leukemic U937 cells, *Life Sci.* 76 (2005) 1623–1639.
- [68] P.E. Czabotar, G. Lessene, A. Strasser, J.M. Adams, Control of apoptosis by the BCL-2 protein family: implications for physiology and therapy, *Nat. Rev. Mol. Cell Biol.* 15 (2014) 49–63.
- [69] J. Kale, E.J. Osterlund, D.W. Andrews, BCL-2 family proteins: changing partners in the dance towards death, *Cell Death Differ.* 25 (2018) 65–80.
- [70] S. Zinkel, A. Gross, E. Yang, BCL2 family in DNA damage and cell cycle control, *Cell Death Differ.* 13 (2006) 1351–1359.